Journal of Neuropathology & Experimental Neurology, 2023, **82**, 57–70
https://doi.org/10.1093/jnen/nlac103
Advance access publication 7 November 2022
Original Article

Postmortem 7T MRI for guided histopathology and evaluation of cerebrovascular disease

David Lahna, BA,[1]* Natalie Roese, MPH,[1] Randy Woltjer, MD, PhD,[1,2] Erin L. Boespflug, PhD,[1] Daniel Schwartz, BA,[1,3] John Grinstead, PhD,[4] Hiroko H. Dodge, PhD,[1,5] Rachel Wall, MS,[1,6] Jeffrey A. Kaye, MD,[1] William D. Rooney, PhD,[3] and Lisa C. Silbert, MD[1,6]

[1]NIA-Layton Alzheimer's Disease Research Center, Oregon Health & Science University, Portland, Oregon, USA
[2]Department of Pathology, Oregon Health & Science University, Portland, Oregon, USA
[3]Advanced Imaging Research Center, Oregon Health & Science University, Portland, Oregon, USA
[4]Siemens Medical Solutions, Malvern, Pennsylvania, USA
[5]Department of Neurology, Massachusetts General Hospital, Harvard Medical School, Boston, Massachusetts, USA
[6]Veterans Affairs Portland Health Care System, Portland, Oregon, USA

*Send correspondence to: David Lahna, BA, Department of Neurology, NIA-Layton Aging and Alzheimer's Research Disease Center, Oregon Health & Science University, 3181 S.W. Sam Jackson Park Road, Portland, OR 97239-3098, USA; E-mail: lahnad@ohsu.edu

ABSTRACT

Postmortem (PM) magnetic resonance imaging (MRI) can serve as a bridge between in vivo imaging and histology by connecting MRI observed macrostructural findings to histological staining and microstructural changes. Data were acquired from 20 formalin-fixed brains including T2, T1, PD, and T2*-weighted images of left hemispheres and 6-mm-thick coronal slices. Tissue slices were bisected, aligned to MR images and used to guide histological sampling. Markers of myelin and oligodendroglia alterations were semiquantitatively rated and compared within white matter hyperintensities (WMHs) and normal-appearing white matter. Tissue priors were created from 3T in vivo data and used to guide segmentation of WMH. PM WMH and hemisphere volumes were compared to volumes derived from in vivo data. PM T2 WMH and T1 hemisphere volumes were correlated with in vivo 3T FLAIR WMH and T1 hemisphere volumes. WMH showed significant myelin loss, decreased GFAP expression and increased vimentin expression. MR-visible perivascular spaces and cortical microvascular lesions were successfully captured on histopathological sections. PM MRI can quantify cerebrovascular disease burden and guide tissue sampling, allowing for more comprehensive characterization of cerebrovascular disease that may be used to study etiologies of age-related cognitive change.

KEYWORDS: 7T MRI, Cerebrovascular disease, Enlarged perivascular spaces, Histology, Neuroimaging, Postmortem, White matter hyperintensity

INTRODUCTION

Cerebrovascular pathologies are common in older adults and are related to poorer cognitive outcomes, including increased risk of mild cognitive impairment and dementia (1–4). Vascular pathologies often co-occur with Alzheimer disease and synergistically lower the threshold for conversion to dementia (5, 6). The full contribution of vascular disease to cognitive impairment is likely underestimated because histopathological sampling strategies may be biased towards neurodegenerative diseases (7), because of variability of observed lesions, and because of a lack of consensus on the significance of neuropathological criteria in the assessment of vascular dementia, vascular cognitive impairment, and related lesions on specific clinical phenotypes (8–12).

Postmortem (PM) magnetic resonance imaging (MRI) is increasingly recognized as a tool for bridging the gap between macrostructural areas of interest observed on in vivo MRI and underlying microstructural pathology (13–18). Compared with in vivo protocols, PM MR sequences can be conducted for longer time periods and at higher resolution, allowing for identification of smaller and more subtle pathology than observed on in vivo scans, which are limited by patient comfort and specific absorption rate concerns. In addition, PM imaging precludes artifacts due to overt motion or motion associated with respiration and vascular pulsatility and enables MRI acquisition in subjects who may not have been able to undergo in vivo imaging due to any number of common exclusions, such as claustrophobia, inability to lie still for prolonged

periods of time, or the presence of implanted metal devices (i.e. permanent pacemaker, etc.).

For those with in vivo MRI, additional PM imaging can capture structural changes that have occurred during the interval between in vivo MRI and death. The importance of the above advantages of PM brain imaging becomes ever more evident in the context of highly characterized research cohorts with longitudinal clinical data who have consented to brain autopsy at death. Conventional histopathological evaluations for cerebrovascular disease (CVD) consist of systematic sampling of standardized brain regions (19), regardless of lesion location, which can vary amongst individuals. PM MRI can identify pathology of interest that may be missed in routine histopathological sampling as well as provide a global survey to accurately assess total brain CVD burden. PM imaging can be used to identify and localize neurological markers of CVD including lacunar infarct, stroke, microbleeds, and white matter hyperintensity (WMH) (20).

WMH are commonly observed on T2-weighted MRI of older individuals and their presence and volume are associated with cognitive and motor impairment, and increased risk of cognitive decline (2, 3, 21). Their etiology has been demonstrated to be primarily vascular in origin although the mechanistic pathogenesis is likely multifactorial and shares relationships with Alzheimer disease pathology (22–24). An MRI pathology study from our group has shown that MRI WMH progression is associated with the presence of cortical neurofibrillary tangles (25), and a subsequent study has supported this relationship (26), reinforcing the notion that both subcortical and cortical pathological states correspond to MR-visible white matter lesions. A more detailed characterization of white matter disease at the cellular level, and how it relates to macroscopic MRI signal change, would facilitate a clearer understanding of these commonly observed in vivo MR findings, and better elucidate WMH as a potentially modifiable biomarker of cognitive impairment in older individuals.

Work in this area has referenced in vivo imaging to examine WMH histology observed in subsequent PM samples (27–33). Early studies describing histological correlates of PM MRI WMHs relied on descriptive MRI WMH measures of presence and location (32, 33). More recent work has quantified WMH PM using visual rating scales on 1.5 or 3T data (28, 30). One study more directly examined histopathological correlates of 3T PM fluid-attenuated inversion recovery (FLAIR) derived WMH, which were found to be spatially related to decreased myelination and vessel density (27). Acquiring data at field strengths higher than 3T would permit for higher resolution acquisitions with shorter scan times, allowing for more precise WMH volumetric quantification and histological targeting of both WMH lesions and its corresponding normal appearing white matter (NAWM) penumbra (34).

Although direct pathological sampling of MR-visible WMH remains infrequent, there is evidence that in addition to axonal loss and white matter rarefaction, WMH may be associated with reactive gliosis (35). Astrocytes in white matter are specialized to support and maintain myelin by secreting pro-myelinating factors and clearing extracellular substances (36). The structural integrity of astrocytes is supported by filamentous proteins, including vimentin and glial acidic fibrillary protein (GFAP), which show increased expression in response to a wide range of neurological diseases and brain damage (37). Increased expression of GFAP has been observed in the WM of patients with CADASIL (cerebral autosomal dominant arteriopathy with subcortical infarcts and leukoencephalopathy), which is characterized by diffuse WMH lesions and multiple infarcts (38). One study directly compared GFAP expression between WMH and NAWM and found increased expression in WMH (39). Despite their potential to elucidate the pathophysiology of WMH, these types of studies remain rare in part due to the methodological difficulty of matching MRI observed lesions with pathology. The precise targeting of tissue guided by MRI is necessary in order to attain the required accuracy to investigate cellular and architectural changes that may differ between the core and the leading edge of MRI-visible WMH or to target other MRI-visible pathologies that are extremely small, such as MRI-visible perivascular spaces (PVS). Furthermore, this type of methodology allows for the direct characterization of areas of interest often observed with in vivo imaging, while avoiding the pitfalls of subjectivity when sampling tissue based solely on pathological abnormalities. Finally, WMH and PVS are just 2 examples of MRI-visible pathologies that are not exclusive to a single neurodegenerative disease; in order to be able to completely differentiate the cellular underpinnings of pathologies that may appear exactly the same on MRI, a streamlined tissue and data handling flow must be employed in order to collect enough objective data in enough subjects to truly provide a complete portrait of the MR-visible pathology in question and make population-wide inferences.

The objective of this study was to optimize a novel 7T protocol for high throughput imaging of PM hemispheres in order to guide histological staining in brain tissue samples obtained from previously active National Institute of Aging (NIA)—Layton Oregon Alzheimer's Research Center (OADRC) participants and to develop a systematic method of presenting histopathologic outcomes. We present a method by which a vast array of MRI-visible pathologies may be isolated and investigated by histopathology using targeted PM 7T MRI, and present results intended to both validate the method as well as pilot results confirming previously detailed characteristics of WMH and enlarged PVS visible on MRI.

MATERIALS AND METHODS

Samples

Left brain hemispheres were obtained from 20 older adults (mean age at death = 94 years; 30% male) who were previ-

Table 1. Subject clinical characteristics

Age at death (years)	94 ± 3.6
Male sex (%)	6 (30)
Education (years of schooling)	15.9 ± 2.3
Alzheimer disease (%)	12 (60)
Vascular dementia (%)	2 (10)
Mixed dementia (%)	5 (25)
Lewy body disease	1 (5)
Postmortem interval (hours)	12.5 ± 20
Fixation to scan interval (months)	7.2 ± 2.3

Figure 1. Whole hemisphere sample preparation for MRI (top) and sliced hemispheres (bottom). Samples are submerged in Fluorinert inside a vacuum sealed container (The ConBrainer). Sample orientation is maintained with interlocking plastic struts (whole hemisphere) or plastic disks with 6-mm spacers (slices.).

ously participating in a longitudinal aging study through the OADRC at Oregon Health & Science University. Both the study participant and their next of kin completed signed autopsy consent, as well as consent for tissue to be used for research purposes. The longitudinal aging study included annual cognitive assessments and the last cognitive assessment for these subjects occurred 0.2–8 years before death (mean- = 1.3 years, SD = 1.77 years). At that assessment 11 (55%) were cognitively intact with a clinical dementia rating (CDR) of 0, 4 had mild cognitive impairment (20%, CDR = 0.5) and 5 had dementia (25%, CDR≥1). Demographic information for study participants including neuropathological diagnoses from the right hemisphere are provided in Table 1.

Tissue preparation

Brains were fixed in a volume approximately equivalent to 4 times the weight of the brain of 13% formalin and imaged in 2 separate scanning sessions, the first sagittally as an intact left hemisphere and then as serial 6-mm-thick coronal tissue slabs.

Hemispheres

Tissue was placed in a plastic vacuum-sealed container for MRI. The hemispheres were oriented within the container so that the sagittal midline of the brain was parallel with the axis of the B0 field and the anterior portion of the brain was upright (mimicking the orientation of supine in vivo imaging). This orientation was maintained using custom fabricated interlocking plastic struts, as shown in Figure 1. The container was filled with Fluorinert (3M, 3M Center, St. Paul, MN) which has the advantage of appearing dark in all MRI sequences. To minimize the presence of bubbles it was vacuum sealed by pumping air out of the container, manually agitated and then left overnight to settle. Manual agitation included turning the sample such that the midline surface was upward and shaking gently to allow air trapped in the anterior portion of the ventricle to escape.

Slices

Following intact hemisphere imaging, the sample was coronally sectioned at 6-mm slices and stored in 13% formalin solution until the sliced tissue imaging session. The 6-mm slices were held in place using a custom fabricated series of 2.38-mm-thick plastic disks threaded onto nylon rods with 6 mm spacers between them (Fig. 1, bottom). The alternating plastic disks and tissue slices were oriented to mimic the intact hemispheres orientation and were held in place by tightening nylon wingnuts onto the ends of the threaded rods. Sixteen 6-mm slices fit into the container, which was enough to include ~65%

of all slices from a hemisphere. The container size was constrained by the size of the available head coil. In the absence of specific lesions of interest observed on whole hemisphere images, we chose to image contiguous slices centered on the ventricles and forego imaging the most anterior and posterior coronal slices in order to retain spatial consistency of the intact hemisphere and maximize the volume of tissue imaged.

Image acquisition

MRI protocol development and acquisition were performed using a Siemens 7 Tesla (T) MAGNETOM. Our 7T imaging protocol was designed to be used to guide targeted histological sampling as well as facilitate coregistration to in vivo data while minimizing scan time. A primary objective was to use MRI of whole hemispheres to scout potential pathology of interest to guide histological sampling, and to quantify total hemisphere CVD burden. This necessitated developing sequences with full hemisphere coverage without slice gaps. Intact hemispheres were imaged sagittally to reduce scan time while sliced tissue was imaged coronally so that the higher in plane resolution matched the coronal tissue slabs (Fig. 2A, B). Full sequence parameters can be found in Table 2.

To allow for coregistration to in vivo data a 0.7-mm isotropic T1-weighted sequence was developed that required shorter inversion and repetition times to account for the shorter T1 of fixed brain tissue. Whole hemisphere coverage of 192 slices were acquired in 11:31 minutes. Additionally, a reference proton density (PD) scan with no inversion pulse was developed and used to correct the T1 volume for B_1 inhomogeneities and T2* contamination (40).

A 2D T2-weighted turbo spin echo sequence was developed with a relatively low turbo factor to minimize blurring from T2 decay and was acquired in 2 runs of 22:55 minutes each for coronal sliced tissue or a single 22:55 minute sagittal run for whole hemisphere coverage.

A 2D T2*-weighted gradient recalled echo sequence was developed with 0.6-mm^3 isotropic resolution to reduce susceptibility artifacts from remaining air bubbles. We also used a high-bandwidth multiecho acquisition (TE1 = 6.89 ms TE2 = 15.8 ms) to further reduce susceptibility artifacts. A monopolar readout gradient was used to avoid susceptibility-induced distortion mismatch between echoes. It was run in 17:24 with 128 slices for sagittal single-hemisphere coverage. We evaluated incorporating a third, longer echo time (TE) at 24.79 ms, but observed qualitatively that the increased extent of artifact due to air bubbles was too severe. This sequence was run exclusively on hemispheres because the artifact from air bubbles trapped between sliced tissue and the supporting plastic was extensive.

Processing

Image processing was completed using tools from the AFNI (41) and FSL (42) packages as specified. T2-weighted images were concatenated in the slice direction to form one contiguous volume. The T1-weighted image was divided by the PD volume (40). N4 Bias field correction was implemented with Slicer (43) and applied separately to the T1 and T2-weighted images. FMRIB's Automated Segmentation Tool (FAST, FSL) was used to isolate the hemisphere from the background of the PD corrected T1 image (44). The sample in the T2-weighted image was segmented from the background using 3dAutomask (AFNI). FMRIB's Linear Image Registration Tool (FLIRT) with 6 degrees of freedom (DOF) was used to coregister T2 to T1 (45).

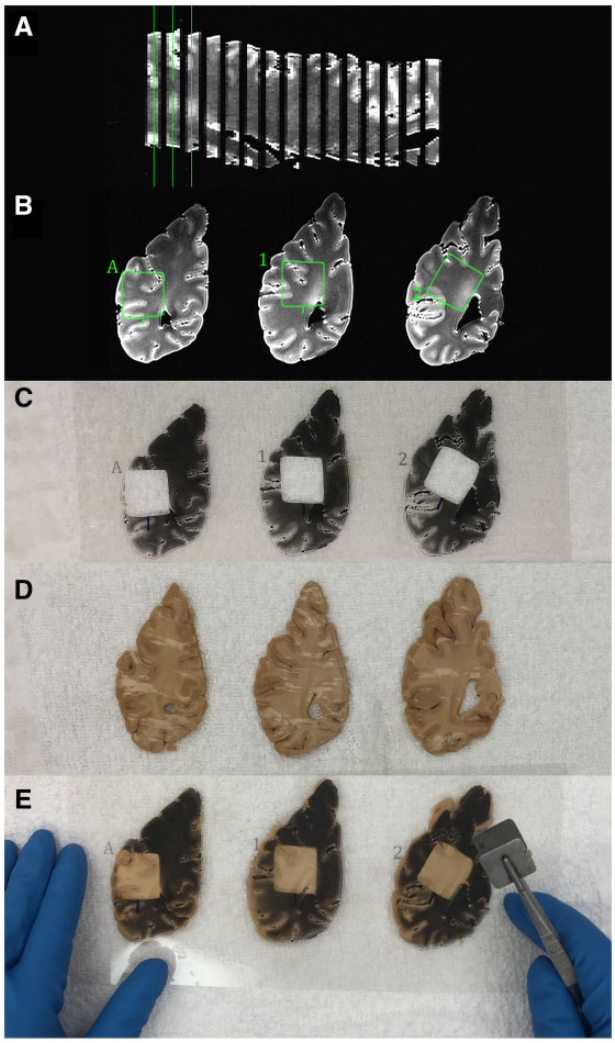

Figure 2. **(A)** T2 sliced tissue MRI, Green lines indicate the center slice used for ROI selection. **(B)** Postmortem T2 MRI montage of slices with selected ROIs. **(C)** Transparencies with ROI cut outs. **(D)** Three-mm-thick coronal tissue slices. **(E)** Tissue with transparency overlay and cutting tool.

WMH segmentation

To aid WMH segmentation a T2-weighted template hemisphere and associated tissue priors were created from in vivo data comprised 88 MR datasets (average age at MRI of 85.9 years, 77.3% female) acquired from subjects participating in an OADRC longitudinal aging study, obtained using 3T MRI (TIM Trio, Siemens Medical Solutions, Malvern, PA). T1-weighted images were acquired using repetition time (TR)=2300 ms, TE = 3.4 ms, inversion time (TI)=1200 ms, spatial resolution of 1 mm isotropic, and 128 slices. Axial 2D FLAIR data sets were acquired using TR = 9000 ms,

Table 2. Sequence parameters

	TR	TE	TI	In-plane resolution (mm)	Slice thickness	No. of slices	Acquisition time (minutes)	Averages	Orientation	Flip angle	Matrix	Echo spacing	Bandwidth	Slice gap
T1	1800 ms	2.44 ms	450 ms	0.7×0.7	0.7 mm	192	11:31	2	Coronal	7°	240×320	6.3 ms	410 Hz/Px	0
PD	1500 ms	2.44 ms		0.7×0.7	0.7 mm	192	9:36	2	Coronal	7°	240×320	6.3 ms	410 Hz/Px	0
T2	5500 ms	52 ms		0.3×0.3	1.2 mm	75	22:55	2	Coronal	180°	736×736	10.3 ms	283 Hz/Px	0
T2*	2000 ms	6.87 ms 15.84 ms		0.6×0.6	0.6 mm	128	17:24	2	Sagittal	90°	368×188		320 Hz/Px	0

Table 3. ROIs sampled histologically using MRI guidance

A	Posterior most slice or horn of the lateral ventricle with nearby white matter and overlying cortex
B	Posterior (to the thalamus) lateral ventricle surface with nearby (periventricular) white matter and overlying cortex
C	Posterior (in same slice as B) PV normal appearing WM with overlying cortex from parietal lobe
D	Posterior (in same slice as B) DEEP normal appearing WM with overlying cortex
E	Globus pallidus, left striatum at anterior commissure
F	Anterior lateral ventricle surface with left cingulate gyrus and corpus callosum (in same slice as E)
G	Anterior relative to "F" PV normal appearing WM with overlying cortex
H	Anterior (in same slice as G) DEEP normal appearing WM with overlying cortex
I	Anterior most slice or horn of the lateral ventricle with nearby white matter and overlying cortex
J	The healthiest white matter from anywhere in the brain

TE = 87 ms, TI = 2500 ms, in-plane resolution was 0.969 mm×0.969 mm, slice thickness = 2 mm, 95 slices. A subset of these subjects (n = 62, mean age at baseline 83.8 years, SD = 8.5 years, 29% male) had longitudinal WMH volumes available from FLAIR based segmentation described previously (46). The WMH growth rate between the first and last visit (mean 2.68 years, SD = 1.7 years) for this cohort was calculated to be 19.9% using a compounding interest formula:

$$r = \left(\frac{F}{B}\right)^{1/t} - 1$$

r = WMH growth rate
F = Followup WMH volume
B = Baseline WMH volume
t = time

T2-weighted datasets were linearly coregistered to T1-weighted images from the same scanning session using FLIRT with 6 DOF. T1-weighted images were segmented into tissue type using Freesurfer (V6.0) and linearly coregistered to the MNI template with 12 DOF. These transforms were then combined and applied to bring T2 data into MNI space for each subject. The coregistered T2 images from all subjects were averaged to form a template and the right hemisphere and the ventricles were removed to mimic the appearance of a PM left hemisphere. Transforms from T1 to MNI space were applied to WM masks which were averaged together creating a WM tissue probability distribution in the same space as the T2 hemisphere template.

Datasets from each subject's PM hemisphere were affine coregistered to the T2 template using FLIRT (FSL) with 12 DOF. T2-weighted images were then multiplied by the WM probability mask resulting in a T2-weighted volume in which voxels unlikely to be in WM appeared darker. Using this dataset as an overlay and the unmodulated but coregistered T2-weighted volume as an underlay, a manual threshold was

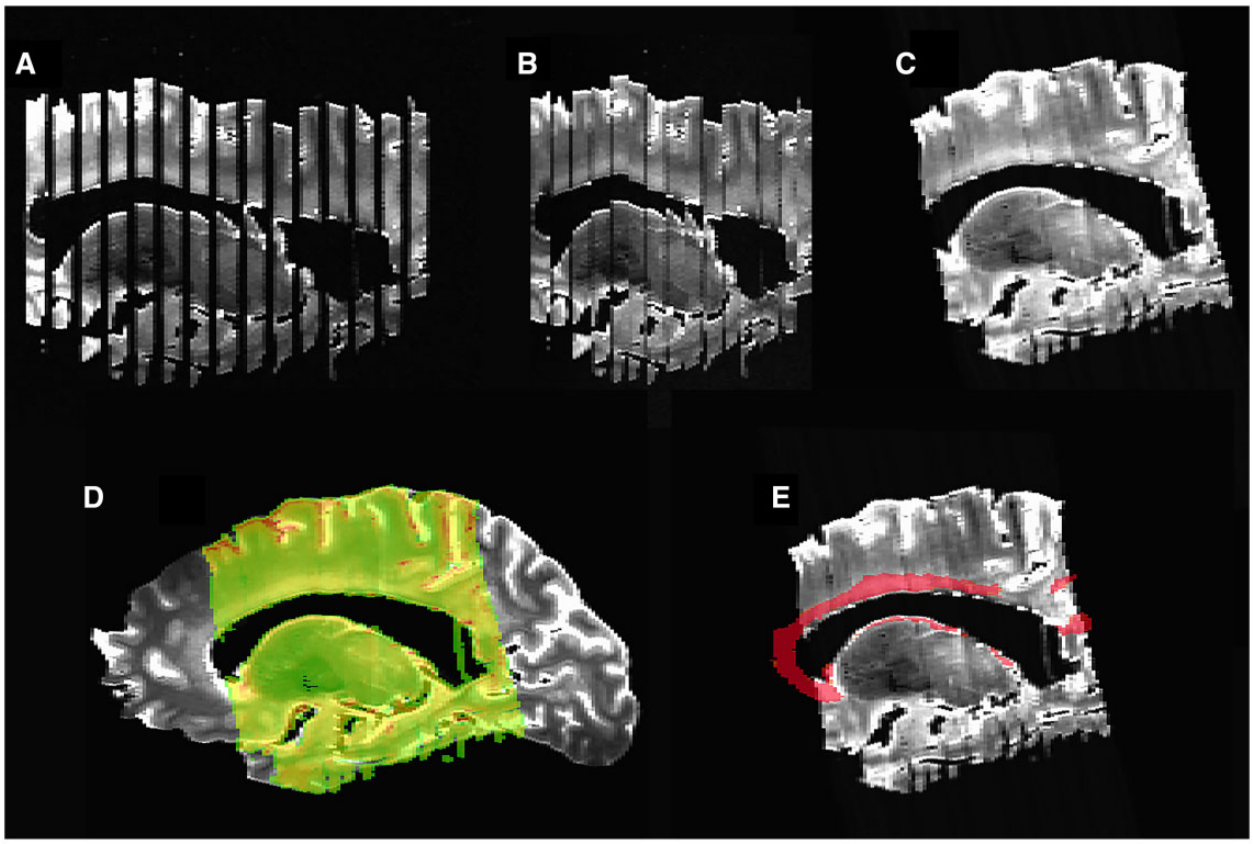

Figure 3. (A) postmortem T2 sagittal view of sliced tissue images. **(B)** T2 sagittal view of sliced tissue images after removal of empty slices and concatenation. **(C)** Sliced tissue images coregistered to the whole hemisphere. **(D)** Overlay of sliced tissue images coregistered to the hemisphere underlay. **(E)** WMH mask derived from hemisphere segmentation, coregistered to sliced data for subsequent MRI-guided histopathological sampling.

chosen so that WMH were mostly included while minimizing GM inclusion. This mask was manually corrected for misclassification errors and brought into native PM hemisphere space to determine WMH volume.

Histological ROI selection and tissue sampling

For each hemisphere, a mosaic image was created from the sliced imaging session by selecting the coronal T2 MRI slice in the center of each 6-mm-thick tissue slab, approximately 3 mm from the outer edges (Fig. 2A). These slices were chosen for ROI selection to: (1) minimize partial volume effects and surface interface artifact because they are furthest from the tissue/plastic surface, and (2) this MR "slice" is most closely spatially related to histological sampling following bisection of the tissue slab. We created a custom cutting tool by sharpening one edge of a sheet of 22-gauge stainless steel and then folding and cutting it down to the size of a histological cassette and affixing a handle. The folding was done so that the cutter had irregular side lengths to aid determination of ROI orientation and then glued together with epoxy. The dimensions of this cutter were converted into MRI voxel dimensions and overlaid on the mosaic image to create a rectangular frame to guide histological sampling (Fig. 2B). The mosaic was then printed to scale on a transparency and the individual ROIs were subsequently cut out with a hobby knife creating a precise guide for our custom tissue cassette cutter (Fig. 2C–E).

Ten regions of interest to be sampled from all brains on the basis of anatomical landmarks were chosen to ensure consistent sampling from each brain (Table 3). Specifically, these consistently sampled regions included those from the anterior and posterior horns of the lateral ventricles, given studies suggesting there may be a pathologically distinct etiology of WMH in anterior vs posterior brain (47). A control region of NAWM was obtained for each sample. Additional samples were chosen based on MRI-identified lesions of interest including WMH, MR-visible PVS, and microvascular lesions (infarcts <2 mm in diameter located in cortex).

Coregistration of PM MRI hemispheres and slices

The average MR signal intensity of each MRI slice parallel to the tissue slabs was calculated using 3dmaskave (AFNI) and slices with average intensity of at least 120% of the minimum average slice intensity were concatenated to form a contiguous volume effectively removing MR slices containing primarily Fluorinert (3M, 3M Center, St. Paul, MN) and plastic (Fig. 3A, B). N4 Bias field correction was applied to both the hemisphere and the concatenated sliced data using Slicer (43). Individual slices in the sliced dataset were registered for slab misalignment with the Fiji (48) plugin StackReg (49) and the

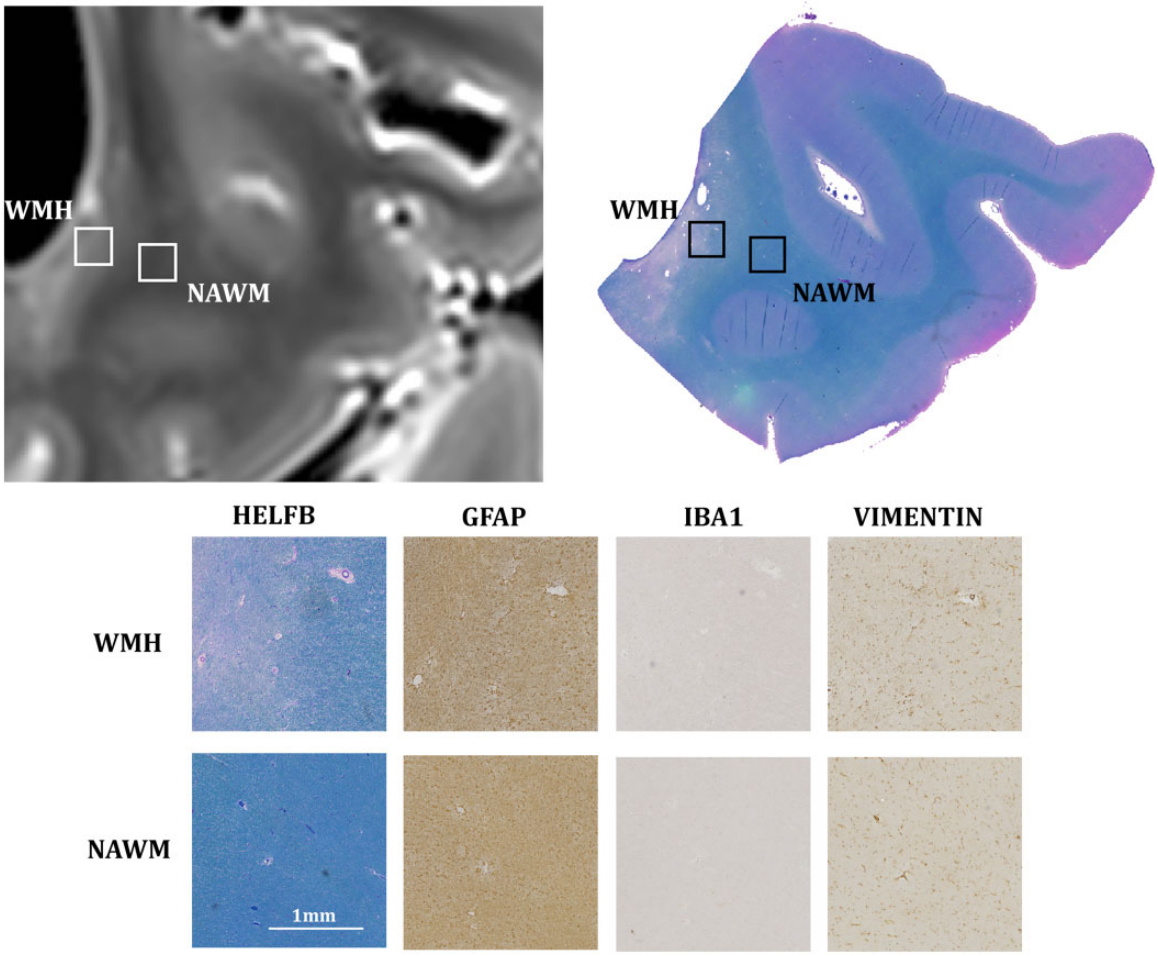

Figure 4. MRI-guided IHC regions of interest selected from white matter hyperintensity and normal appearing white matter.

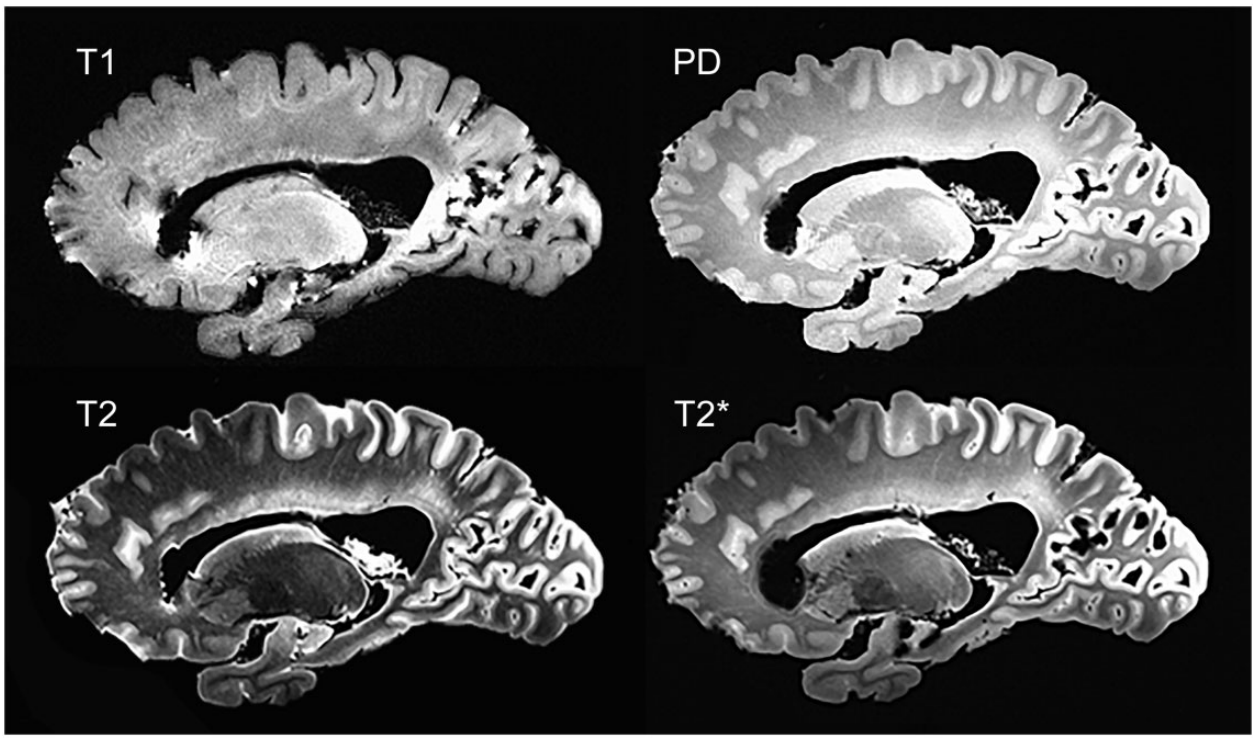

Figure 5. Whole hemisphere postmortem data acquired at 7T and coregistered.

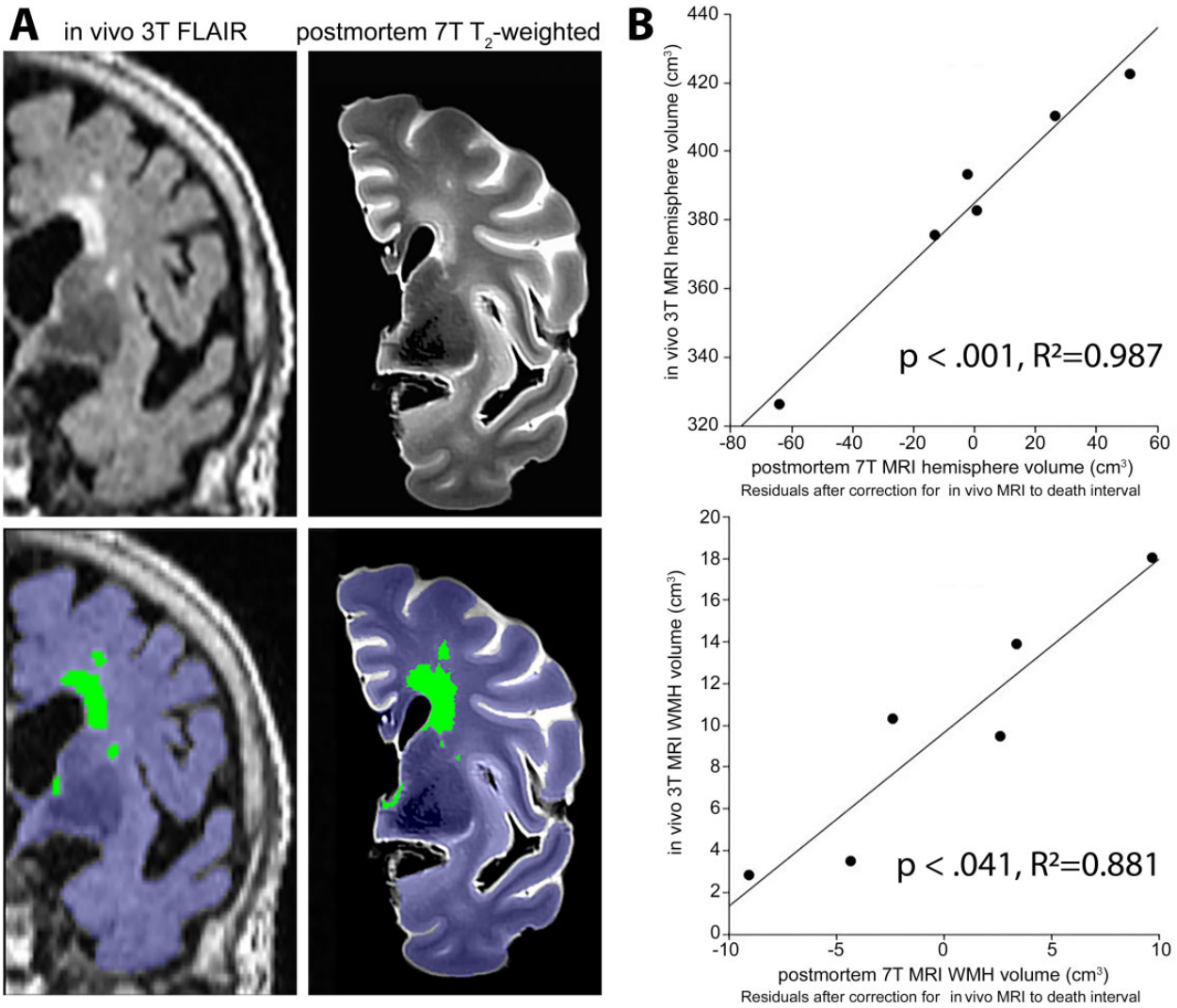

Figure 6. **(A)** WMH and hemisphere segmentation from the same subject in coregistered FLAIR in vivo 3.7 years before death (left) and T2 postmortem (right). **(B)** Top: Relationship between in vivo 3T MRI hemisphere volume and postmortem hemisphere volume after correction for interval between in vivo MRI and death. Bottom: Relationship between in vivo 3T MRI WMH volume and postmortem WMH volume after correction for interval between in vivo MRI and death.

center of mass of the slice dataset was aligned to that of the hemisphere dataset with @Align_Centers (AFNI). The slice dataset was registered to the hemisphere dataset using the ANTS program antsRegistrationSyNQuick (50) (Fig. 3C, D). The inverse transformation was then applied to the hemisphere and associated WMH mask (Fig. 3E).

In vivo coregistration

A subset of study participants with PM MRI had also undergone in vivo 3T MRI as part of their participation in an OADC longitudinal neuroimaging study (n = 6), with acquisition parameters as previously described (34). PM images were coregistered to in vivo data to test the stability of WMH, hemispheric volumes, and enlarged PVS (ePVS) detection pre- and postmortem. The in vivo T1 coregistration target was skull stripped as part of the Freesurfer (v6.0) pipeline. The right hemisphere of the image was masked out at the midline and resampled to a higher resolution (0.3 mm isotropic). 3dAllineate (AFNI) with 12 DOF was used to calculate the affine transform from PM to in vivo T1.

Semiquantitative immunohistochemistry WMH analysis

Five cassettes (Table 3) each from 6 hemispheres were targeted for comparison of immunohistochemistry (IHC) markers of myelin and oligodendroglial alterations between WMH and NAWM. Immunohistochemistry was performed after deparaffinized sections were subjected to antigen retrieval (5-minute treatment at room temperature with 95% formic acid followed by incubation at 85–90°C in citrate buffer, pH 6.0 for 30 minutes) to detect glial fibrillary acidic protein (GFAP), ionized calcium binding adapter molecule-1 (IBA1), and vimentin using antibodies from Proteintech (Rosemont, IL) (GFAP, vimentin) and Wako USA (Richmond, VA) according to the manufacturer's instructions. Slides were scanned with Zeiss Axio Slide Scanner at 5× resolution. CZI images were downsampled 24% and exported as PNGs. Sliced

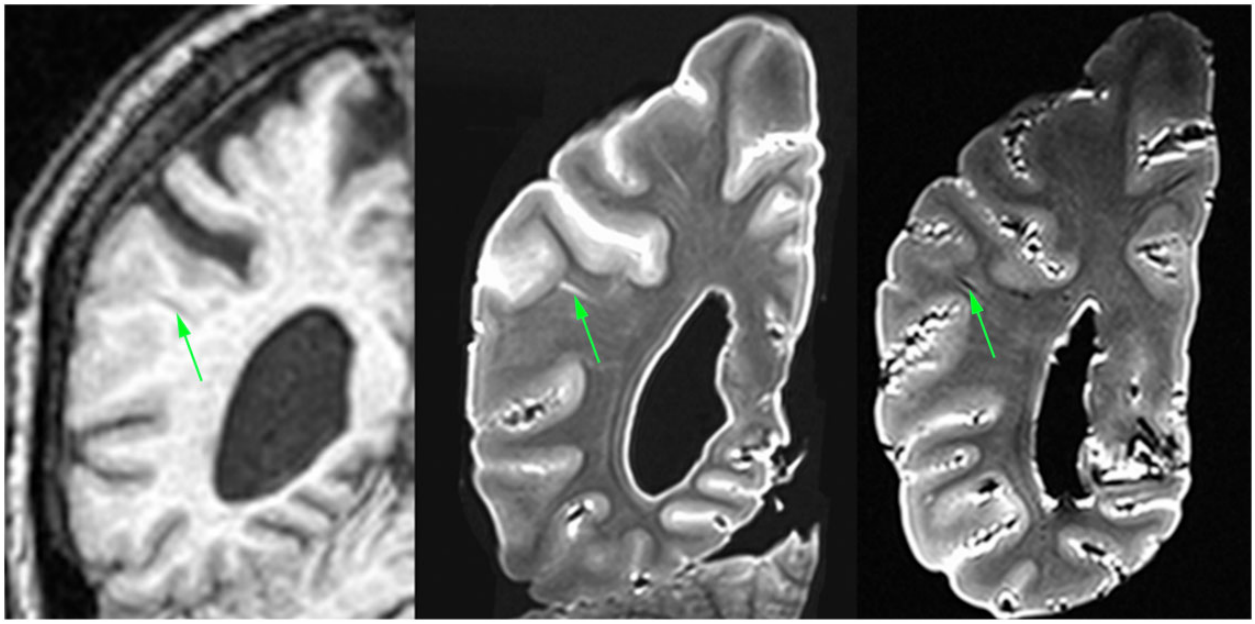

Figure 7. Enlarged perivascular space in in vivo 3T T1 (left), postmortem 7T hemisphere T2 (center) and postmortem 7T slice T2 (right).

T2 MRI, Hemisphere T2 MRI (registered to be in Slice space) and associated WM, GM and WMH masks and downsampled PNGs were loaded into MATLAB and the slices and corresponding PNGs were interactively aligned. Twenty-five square (2 mm×2 mm) regions of interest were selected from within WMH masks derived from coregistered PM MRI as well as 25 corresponding nearby ROIs of NAWM (Fig. 4). An experienced neuroradiologist (R.Wo.) blinded to the WMH/NAWM designation rated the ROIs on a 0–3 point scale for myelin pallor (HELFB), location of astrocyte process expression (GFAP), degree of expression (IBA1), and degree of glial expression (vimentin).

Statistics

Semiquantitative IHC ratings between WMH and NAWM were compared using a Wilcoxon signed-rank (S-R) test. Associations between PM hemisphere volumes and brain weight, PM interval, and fixation duration were examined using multiple linear regressions. Relationships between PM volumes of interest (left hemisphere, WMH) and corresponding in vivo volumetrics, were examined using multivariate linear regression models, adjusted for time interval between in vivo MRI and death. Pearson correlation was used to test the accuracy of PM WMH segmentations against estimates based on the WMH growth rate for the cohort derived from in vivo data.

RESULTS

A sample representation of the described multimodal PM protocol can be found in Figure 5. Pathology identified on 3T in vivo MRI was verified in PM 7T MRI, and included WMH (Fig. 6A) and ePVS (Figs. 7 and 8). These lesions of interest, as well as several microvascular infarcts identified on PM hemisphere 7T imaging (Fig. 9), were successfully targeted using histology with MRI guidance.

PM MRI hemisphere volumetrics

Multiple linear regression was used to predict PM hemisphere volume based on brain weight at autopsy, time interval between death and fixation and the duration of fixation. A significant regression equation was found ($F(3,16)=7.302$, $p < 0.003$) with an R^2 of 0.499 (Fig. 10). Brain weight was a significant predictor of hemisphere volume ($p<0.007$). The interval between death and fixation ($p=0.564$) and the fixation duration ($p=0.303$) were not significant predictors of hemisphere volume. Brain weight was found to be .241 grams higher for each $1mm^3$ increase in PM fixed hemisphere volume.

Multiple linear regression was also used to predict PM hemisphere volume based on the in vivo hemisphere volume ($n = 6$) and the time interval in years between in vivo MRI and death. A significant regression equation fit ($F(2,3)=114.286$), $p<0.001$) with an R^2 of 0.987 (Fig. 6B, top). In vivo hemisphere volume ($p<0.001$) and the interval between in vivo MRI and death ($p<0.003$) were significant predictors of PM hemisphere volume.

PM MRI WMH volumetrics

Multiple linear regression was also used to predict PM WMH volume from T2 segmentation based on in vivo FLAIR WMH volume ($n = 6$) and the time interval between in vivo MRI and death (Fig. 6B). A significant regression equation fit ($F(2,3)=11.08$, $p < 0.041$) with an R^2 of 0.881. In vivo WMH volume was a significant predictor of PM WMH volume ($p < 0.018$). The time interval between in vivo MRI and death was not significant ($p = 0.445$).

PM WMH values were not significantly correlated with the projections based on baseline in vivo WMH volumes and the growth rate for this cohort ($n = 6$, $p = 0.074$, Pearson $R = 0.769$). However, upon closer examination one sample was found to have significantly larger WMH PM than pre-

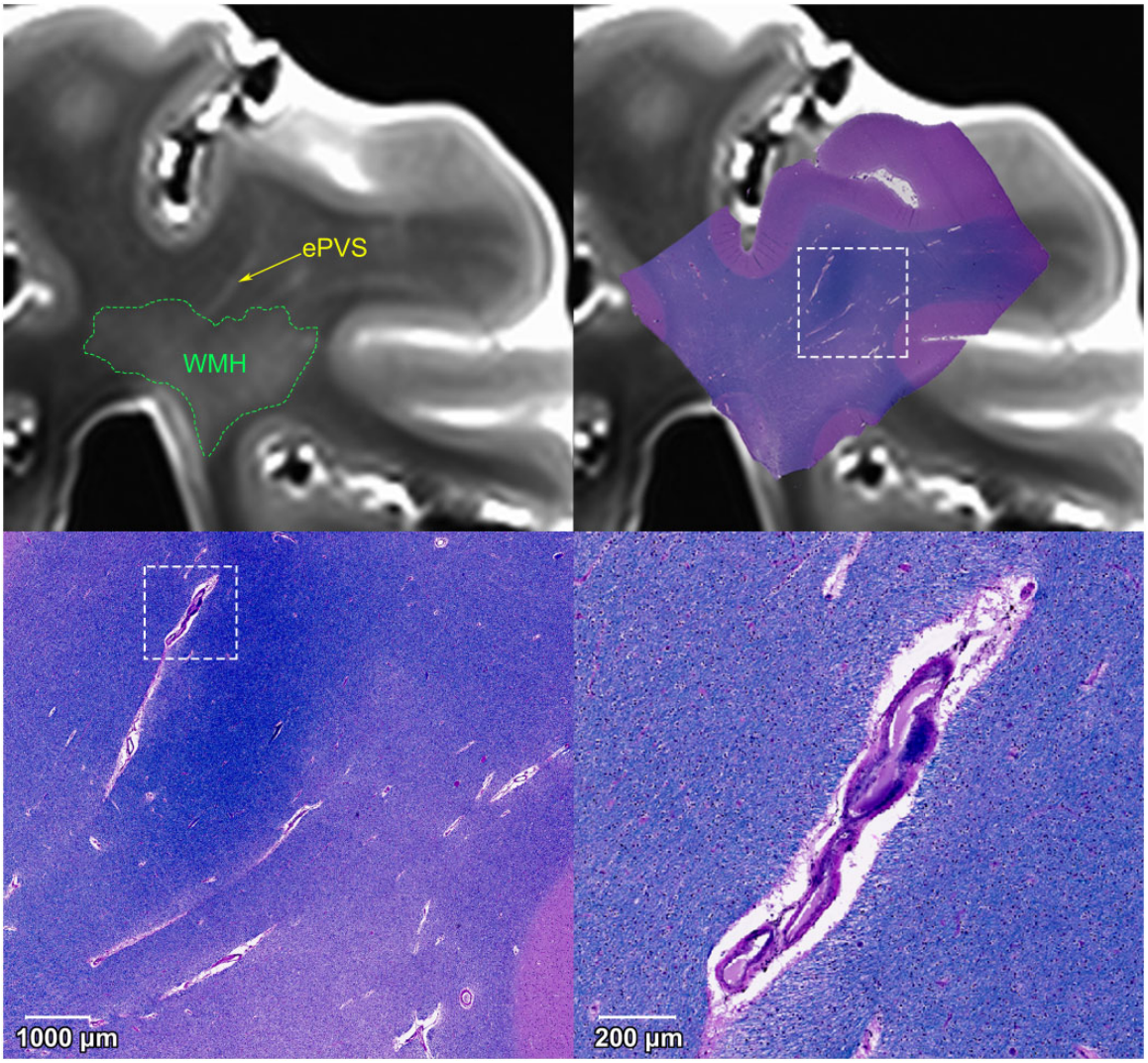

Figure 8. Top left: Postmortem T2 with visible enlarged perivascular space (ePVS) and white matter hyperintensity (WMH). Top right: H&E-stained histological section coregistered to postmortem T2. Bottom: increased magnification of ePVS and WMH on H&E.

dicted due to a large stroke (the cause of death). With this subject excluded the WMH projections were significantly correlated with PM MRI segmented volumes ($n = 5$, $p < 0.026$, Pearson $R = 0.922$) (Fig. 11).

Region of interest analysis

WMH evidenced significantly higher myelin pallor on H&E-LFB ($p = 0.0008$), more proximal GFAP expression ($p = 0.009$), and increased vimentin glial expression ($p = 0.0001$) compared to NAWM (Fig. 12). No significant difference was observed in IBA1 expression between NAWM and WMH regions of interest.

DISCUSSION

Acquisition

We present a PM high-field 7T MR data acquisition protocol that can detect CVD-associated pathology including WMH, ePVS, and microvascular lesions at high resolution as well as quantify WMH and hemisphere volumes, using a relatively short acquisition time of 62 minutes. T1 data were susceptible to fixation artifact and B_1 inhomogeneity, which, while partially corrected for using a PD reference scan, could not be entirely accounted for. The T2-weighted sequence in particular allowed for the greatest clarity of pathological identification of CVD as it had the highest in plane resolution and demonstrated less fixation artifact and artifact from air bubbles.

Processing

Coregistration of PM to in vivo T1-weighted data using publicly available, commonly used algorithms was generally successful at accounting for shape changes with 2 notable exceptions. Poorer registration around the ventricles was observed, which is likely the result of both ventricular expansion encountered in older populations, especially with neurodegenerative diseases, and the absence of CSF pressure PM making the tissue susceptible to physical deformation. A nonlinear compression of the PM hemisphere in the anterior to posterior direction was inadvertently introduced when trying to fit especially large hemispheres into the container. In these

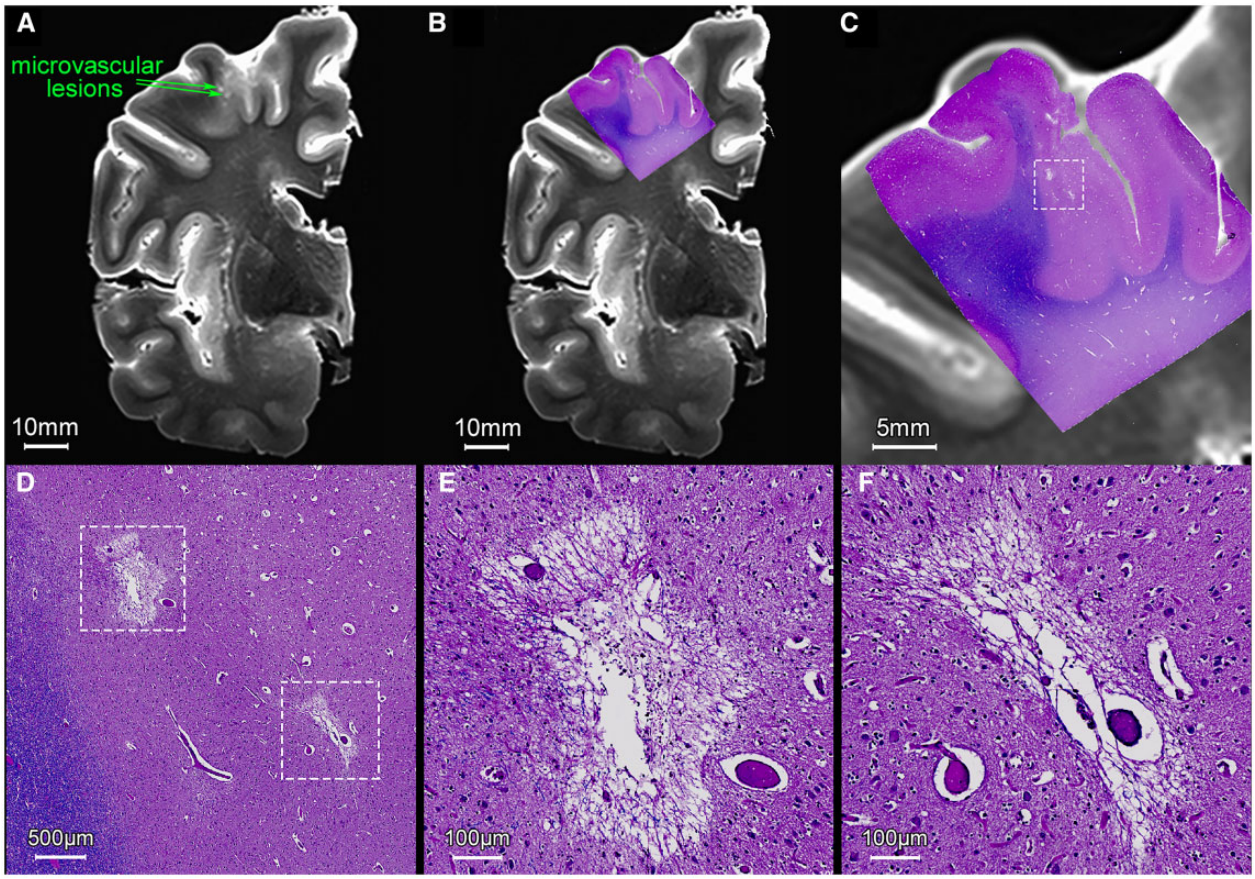

Figure 9. **(A)** Microvascular lesions visible in T2 postmortem MRI. **(B)** Coregistered H&E-stained slide. **(C)** Increased magnification of coregistered H&E. **(D)** Microvascular lesions targeted with postmortem MRI and stained with H&E. **(E, F)** Increased magnification of microvascular lesions.

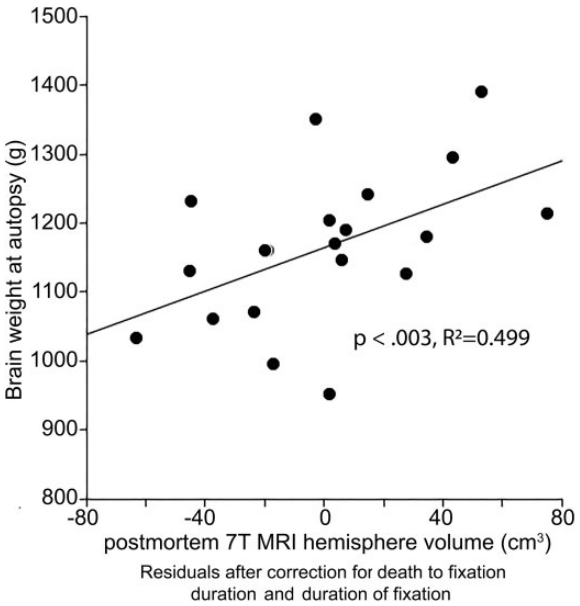

Figure 10. Whole brain weight at autopsy is a significant predictor of left hemisphere volume from postmortem imaging in a regression model accounting for the duration of fixation and the time interval between death and fixation.

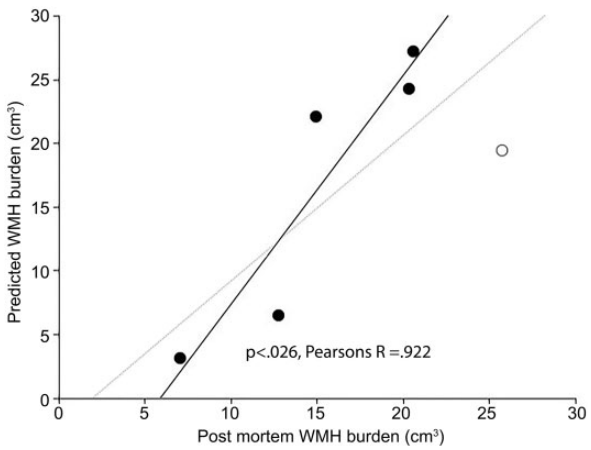

Figure 11. Correlation between predicted postmortem WMH volumes and measured WMH volume. Predictions were made using baseline in vivo measurements of WMH volume, the known WMH growth rate for this cohort and the time interval between in vivo MRI and death. One sample (white circle) deviated significantly from the prediction due to a large stroke at death which increased the WMH burden.

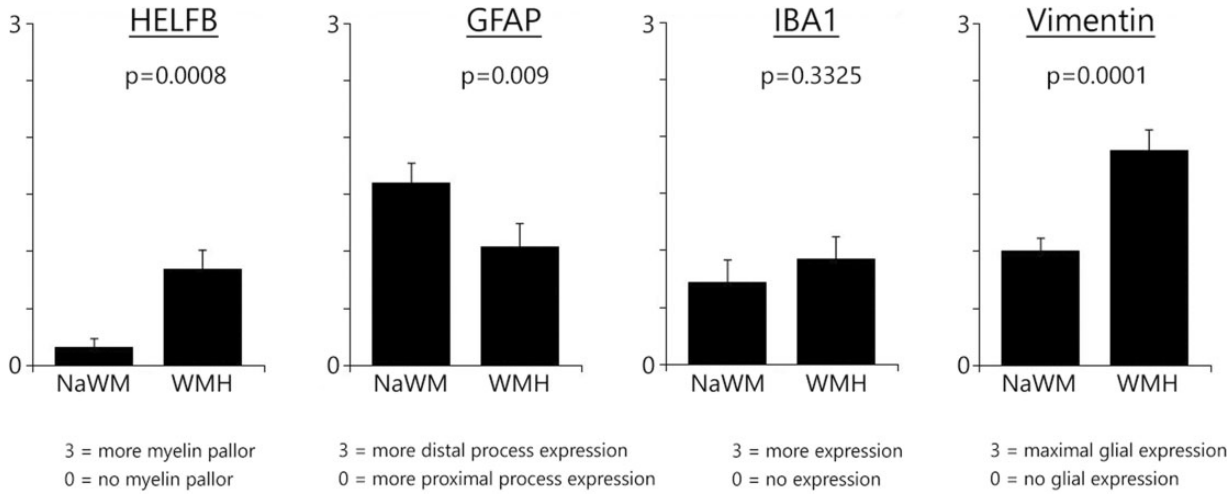

Figure 12. Wilcoxon signed-rank tests between NAWM and WMH on ratings of histological characteristics pertinent to each stain.

instances, the frontal lobe was compressed by the buoyancy pressure on the brain against the flat plastic plate holding it down. This type of nonlinear compression could not be accounted for using linear coregistration methods. Using a larger container would be ideal although the container size is limited by the available MRI coil volume.

Volumetrics

PM hemisphere volumes were correlated with in vivo hemisphere volumes as well as brain weight at autopsy. PM hemisphere volumes calculated using this protocol may serve as a useful biomarker of neurodegeneration and pathological volume loss that might be used to validate in vivo biomarkers.

WMH volumes calculated from PM MRI of brain hemispheres were commensurate with in vivo WMH volumes for the subset in which in vivo data were available. In addition, the PM-derived WMH volumes were in line with estimates based on WMH growth rates for this cohort derived from in vivo longitudinal imaging. Despite the application of tissue priors for this population derived from in vivo data, manual correction was still required to ensure accuracy of WMH masks. Future work may be able to better automate this process using improved multimodal tissue segmentation and deep learning algorithms. Despite this, results from this study validates the use of PM MRI to assess global WMH burden and cortical microinfarcts that may not be available or observed on in vivo MRI or fully captured on standard histopathological sections.

Histological guidance

One aim of this protocol development is to guide histological sampling using the PM MRI by placing ROIs on the center MRI slice of the T2 images containing MRI visible pathology of interest (Fig. 3). This approach allowed us to identify WMH and ePVS in regions that may have been overlooked in a standard pathological analysis with predetermined anatomical ROI sampling. The ability to identify ePVS in intact tissue will be important in mitigating concern over tissue retraction in standard tissue preparation, which may create cavities around vessels that mimic ePVS. In order to directly compare histological images to MRI images, which are 1.2 mm thick, one would need to average 240, 5-µm-thick histological slides. For this reason, pathology that is MRI visible may still be missing from stained slides even with guidance; for example, a clearly enlarged linear ePVS on MRI may be transected and appear circular on histology. Thus, while we cannot always precisely isolate a single vessel or WMH, this method will consistently allow sampling of regions that appear enriched for the pathology of interest and increase the likelihood that it will be captured in a histological section.

Immunohistochemistry of MRI-guided sampling comparing WMH and NAWM

The observed significant difference in myelin pallor as evidenced by HELFB staining within MRI targeted WMH and NAWM provides confirmation of the accuracy of the sampling method developed here. We had hypothesized that WMH would be characterized by an increase in markers of astrocytopathy. A pathological distribution of GFAP expression was observed in the WMH compared to NAWM, with expression of the protein being relocated to a more proximal location on the cell processes relative to the cell body in WMH. Though no difference in IBA1 expression was observed, an increase in glial expression of vimentin was significant.

One plausible explanation for these findings is that MRI visible WMH ROIs in this sample of oldest old individuals, with the mean age at death being 94 years, represent the very latest stages of WM tissue destruction, when cellular deterioration precludes the ability to fully interpret the lack of histochemical staining. It is also possible that GFAP changes precede changes in vimentin, which may persist for longer in the disease process. Finally, this group and others have found that while the overall level of GFAP staining in WMH (and in NAWM) can be quite variable, invariably GFAP exhibits a pattern in WMH much like what is shown in Figure 4, that is that astrocyte processes have retracted towards cell bodies and some fine processes have been lost (51, 52), resulting in a more heterogeneous profile across the slide. Astrocyte cell bodies and the immediate surrounding (retracted) processes

exhibit increased GFAP expression in WMH than NAWM though less of the tissue displays positive staining, as opposed to the more diffuse and inclusive staining of extended and undamaged astrocytic processes seen throughout the parenchyma in NAWM.

Future efforts will include the assessment of astrocytic markers within the NAWM surrounding WMHs (the WMH penumbra), where white matter tissue integrity has been shown to be impacted to a lesser degree than WMH lesions themselves on in vivo imaging. A likely continuum of age and ischemia-related WM pathologies within and surrounding WMH lesions will be better captured in this way. Future work involving the counting of nonreactive astrocytes and comparing the ratio of GFAP+ to normal astrocytes between WMH and NAWM is also needed.

In summary, we present a 7T PM imaging acquisition and processing framework that allows for a hemispheric survey of areas of interest, including brain size and WMH burden on which volumetry can be reliably performed. The described additional imaging of sliced tissue that serves to identify ROIs based on the presence of MRI visible pathologies and subsequent tissue dissection for histopathological sampling allows for specific targeting of MRI-identified ROIs for detailed histopathological characterization. This methodology allows for the study of currently validated MRI biomarkers, such as quantification of whole hemisphere brain volume, ePVS, microvascular lesions or WMH in valuable research cohorts who have been highly characterized in life, but who may not have undergone in vivo MRI. Importantly, this methodology allows for the more specific targeting of areas of interest that have yet to be histopathologically defined by direct sampling. These methods were originally developed for the purpose of studying histopathological correlates of age and dementia-related PM MRI biomarkers in an OADRC longitudinal study cohort to describe the molecular underpinnings of CVD-related MRI markers and their relationship to dementia risk. They are directly translatable, however, into histopathological studies of other diseases characterized by MRI-visible pathologies of interest (e.g. multiple sclerosis) to facilitate a more detailed understanding of molecular pathologies driving disease processes and underlying MR-observed lesions common in life, and describe an efficient, high-throughput tissue sample and data flow regime to facilitate objective data collection at a scale necessary for population-wide inference.

FUNDING

This project was supported by the NIH (R01 AG056712, P30AG066518, P30AG008017, R01 AG036772, K01 AG059842, P30 NS061800) and the Department of Veterans Affairs.

CONFLICT OF INTEREST

The authors have no duality or conflicts of interest to declare.

REFERENCES

1. DeCarli C, Murphy DG, Tranh M, et al. The effect of white matter hyperintensity volume on brain structure, cognitive performance, and cerebral metabolism of glucose in 51 healthy adults. Neurology 1995;45:2077–84
2. Silbert LC, Nelson C, Howieson DB, et al. Impact of white matter hyperintensity volume progression on rate of cognitive and motor decline. Neurology 2008;71:108–13
3. Silbert LC, Howieson DB, Dodge H, et al. Cognitive impairment risk: White matter hyperintensity progression matters. Neurology 2009;73:120–5
4. Debette S, Markus HS. The clinical importance of white matter hyperintensities on brain magnetic resonance imaging: Systematic review and meta-analysis. BMJ 2010;341:c3666
5. Vemuri P, Lesnick TG, Przybelski SA, et al. Vascular and amyloid pathologies are independent predictors of cognitive decline in normal elderly. Brain 2015;138:761–71
6. Attems J, Jellinger KA. The overlap between vascular disease and Alzheimer's disease–lessons from pathology. BMC Med 2014;12:206
7. Love S, Miners JS. Small vessel disease, neurovascular regulation and cognitive impairment: Post-mortem studies reveal a complex relationship, still poorly understood. Clin Sci (Lond) 2017;131:1579–1589
8. Grinberg LT, Heinsen H. Toward a pathological definition of vascular dementia. J Neurol Sci 2010;299:136–8
9. Sachdev P, Kalaria R, O'Brien J, et al.; International Society for Vascular Behavioral and Cognitive Disorders. Diagnostic criteria for vascular cognitive disorders: A VASCOG statement. Alzheimer Dis Assoc Disord 2014;28:206–18
10. Kalaria RN. Neuropathological diagnosis of vascular cognitive impairment and vascular dementia with implications for Alzheimer's disease. Acta Neuropathol 2016;131:659–85
11. Hyman BT, Phelps CH, Beach TG, et al. National Institute on Aging-Alzheimer's Association guidelines for the neuropathologic assessment of Alzheimer's disease. Alzheimers Dement 2012;8:1–13
12. Montine TJ, Phelps CH, Beach TG, et al.; Alzheimer's Association. National Institute on Aging-Alzheimer's Association guidelines for the neuropathologic assessment of Alzheimer's disease: A practical approach. Acta Neuropathol 2012;123:1–11
13. Dal-Bianco A, Grabner G, Kronnerwetter C, et al. Slow expansion of multiple sclerosis iron rim lesions: Pathology and 7 T magnetic resonance imaging. Acta Neuropathol 2017;133:25–42
14. Kolasinski J, Stagg CJ, Chance SA, et al. A combined post-mortem magnetic resonance imaging and quantitative histological study of multiple sclerosis pathology. Brain 2012;135:2938–51
15. Schmierer K, Wheeler-Kingshott CA, Tozer DJ, et al. Quantitative magnetic resonance of postmortem multiple sclerosis brain before and after fixation. Magn Reson Med 2008;59:268–77
16. De Reuck J, Auger F, Durieux N, et al. Frequency and topography of small cerebrovascular lesions in vascular and in mixed dementia: A post-mortem 7-Tesla magnetic resonance imaging study with neuropathological correlates. Folia Neuropathol 2017;55:31–37
17. Haller S, Montandon ML, Lazeyras F, et al. Radiologic-histopathologic correlation of cerebral microbleeds using pre-mortem and post-mortem MRI. PLoS One 2016;11:e0167743
18. Pallebage-Gamarallage M, Foxley S, Menke RAL, et al. Dissecting the pathobiology of altered MRI signal in amyotrophic lateral sclerosis: A post mortem whole brain sampling strategy for the integration of ultra-high-field MRI and quantitative neuropathology. BMC Neurosci 2018;19:11
19. Besser LM, Kukull WA, Teylan MA, et al. The Revised National Alzheimer's Coordinating Center's neuropathology form-available data and new analyses. J Neuropathol Exp Neurol 2018;77:717–726

20. McAleese KE, Alafuzoff I, Charidimou A, et al. Post-mortem assessment in vascular dementia: Advances and aspirations. BMC Med 2016;14:129
21. Silbert LC, Dodge HH, Perkins LG, et al. Trajectory of white matter hyperintensity burden preceding mild cognitive impairment. Neurology 2012;79:741–7
22. Alosco ML, Sugarman MA, Besser LM, et al. A clinicopathological investigation of white matter hyperintensities and Alzheimer's disease neuropathology. J Alzheimers Dis 2018;63:1347–1360
23. Erten-Lyons D, Woltjer R, Kaye J, et al. Neuropathologic basis of white matter hyperintensity accumulation with advanced age. Neurology 2013;81:977–83
24. Shim YS, Yang DW, Roe CM, et al. Pathological correlates of white matter hyperintensities on magnetic resonance imaging. Dement Geriatr Cogn Disord 2015;39:92–104
25. Erten-Lyons D, Dodge HH, Woltjer R, et al. Neuropathologic basis of age-associated brain atrophy. JAMA Neurol 2013;70:616–22
26. McAleese KE, Firbank M, Dey M, et al. Cortical tau load is associated with white matter hyperintensities. Acta Neuropathol Commun 2015;3:60
27. Murray ME, Vemuri P, Preboske GM, et al. A quantitative post-mortem MRI design sensitive to white matter hyperintensity differences and their relationship with underlying pathology. J Neuropathol Exp Neurol 2012;71:1113–22
28. Munoz DG, Hastak SM, Harper B, et al. Pathologic correlates of increased signals of the centrum ovale on magnetic resonance imaging. Arch Neurol 1993;50:492–7
29. Fernando MS, O'Brien JT, Perry RH, et al.; Neuropathology Group of MRC CFAS. Comparison of the pathology of cerebral white matter with post-mortem magnetic resonance imaging (MRI) in the elderly brain. Neuropathol Appl Neurobiol 2004;30:385–95
30. Young VG, Halliday GM, Kril JJ. Neuropathologic correlates of white matter hyperintensities. Neurology 2008;71:804–11
31. Grinberg LT, Amaro Junior E, da Silva AV, et al.; Brazilian Aging Brain Study Group. Improved detection of incipient vascular changes by a biotechnological platform combining post mortem MRI in situ with neuropathology. J Neurol Sci 2009;283:2–8
32. Marshall VG, Bradley WG Jr, Marshall CE, et al. Deep white matter infarction: Correlation of MR imaging and histopathologic findings. Radiology 1988;167:517–22
33. Braffman BH, Zimmerman RA, Trojanowski JQ, et al. Brain MR: Pathologic correlation with gross and histopathology. 2. Hyperintense white-matter foci in the elderly. AJR Am J Roentgenol 1988; 151:559–66
34. Promjunyakul N, Lahna D, Kaye JA, et al. Characterizing the white matter hyperintensity penumbra with cerebral blood flow measures. Neuroimage Clin 2015;8:224–9
35. Wardlaw JM, Valdes Hernandez MC, Munoz-Maniega S. What are white matter hyperintensities made of? Relevance to vascular cognitive impairment. J Am Heart Assoc 2015;4:001140
36. Lundgaard I, Osorio MJ, Kress BT, et al. White matter astrocytes in health and disease. Neuroscience 2014;276:161–73
37. Hol EM, Capetanaki Y. Type III intermediate filaments desmin, glial fibrillary acidic protein (GFAP), vimentin, and peripherin. Cold Spring Harb Perspect Biol 2017;9:a021642
38. Hase Y, Chen A, Bates LL, et al. Severe white matter astrocytopathy in CADASIL. Brain Pathol 2018;28:832–843
39. Gouw AA, Seewann A, Vrenken H, et al. Heterogeneity of white matter hyperintensities in Alzheimer's disease: Post-mortem quantitative MRI and neuropathology. Brain 2008;131:3286–3298
40. Van de Moortele PF, Auerbach EJ, Olman C, et al. T1 weighted brain images at 7 Tesla unbiased for proton density, T2 contrast and RF coil receive B1 sensitivity with simultaneous vessel visualization. Neuroimage 2009;46:432–46
41. Cox RW. AFNI: Software for analysis and visualization of functional magnetic resonance neuroimages. Comput Biomed Res 1996;29:162–73
42. Smith SM, Jenkinson M, Woolrich MW, et al. Advances in functional and structural MR image analysis and implementation as FSL. Neuroimage 2004;23(Suppl 1):S208–19
43. Tustison NJ, Avants BB, Cook PA, et al. N4ITK: Improved N3 bias correction. IEEE Trans Med Imaging 2010;29:1310–20
44. Zhang Y, Brady M, Smith S. Segmentation of brain MR images through a hidden Markov random field model and the expectation-maximization algorithm. IEEE Trans Med Imaging 2001;20:45–57
45. Jenkinson M, Smith SA. Global optimisation method for robust affine registration of brain images. Med Image Anal 2001;5:143–56
46. Promjunyakul NO, Dodge HH, Lahna D, et al. Baseline NAWM structural integrity and CBF predict periventricular WMH expansion over time. Neurology 2018;90:e2119–26
47. Brickman AM, Zahodne LB, Guzman VA, et al. Reconsidering harbingers of dementia: Progression of parietal lobe white matter hyperintensities predicts Alzheimer's disease incidence. Neurobiol Aging 2015;36:27–32
48. Schindelin J, Arganda-Carreras I, Frise E, et al. Fiji: An open-source platform for biological-image analysis. Nat Methods 2012;9: 676–82
49. Thevenaz P, Ruttimann UE, Unser MA. Pyramid approach to subpixel registration based on intensity. IEEE Trans Image Process 1998;7:27–41
50. Avants BB, Tustison NJ, Song G, et al. A reproducible evaluation of ANTs similarity metric performance in brain image registration. Neuroimage 2011;54:2033–44
51. Kim R, Healey KL, Sepulveda-Orengo MT, et al. Astroglial correlates of neuropsychiatric disease: From astrocytopathy to astrogliosis. Prog Neuropsychopharmacol Biol Psychiatry 2018; 87:126–146
52. Pekny M, Pekna M, Messing A, et al. Astrocytes: A central element in neurological diseases. Acta Neuropathol 2016;131:323–345